Structural and magnetic phase diagram of the two-electron-doped $(Ca_{1-x}Ce_x)MnO_3$ system: Effects of competition among charge, orbital, and spin ordering

El'ad N. Caspi,* Maxim Avdeev, Simine Short, and James D. Jorgensen

Materials Science Division, Argonne National Laboratory, Argonne, Illinois 60439, USA

Maxim V. Lobanov, Zuotao Zeng, and Martha Greenblatt

Department of Chemistry and Chemical Biology, Rutgers, the State University of New Jersey, Piscataway, New Jersey 08854, USA

Pappannan Thiyagarajan

Intense Pulsed Neutron Source, Argonne National Laboratory, Argonne, Illinois 60439, USA

Cristian E. Botez and Peter W. Stephens

Department of Physics & Astronomy, State University of New York, Stony Brook, New York 11794, USA

The crystallographic and magnetic phase diagram of the two-electron-doped system $(Ca_{1-x}^{2+}Ce_x^{4+})MnO_3$ with $0 \leq x \leq 0.167$ has been determined using neutron powder diffraction, synchrotron x-ray powder diffraction, small angle scattering, and ac susceptibility. In general, the phase diagram is similar to those for other chemically substituted $CaMnO_3$ systems as viewed as a function of the Mn charge state. Thus, when viewed as a function of the Ce concentration x the phase diagram is compressed by a factor of 2. Particular differences, such as a broad compositional region ($0.1 \leq x \leq 0.167$) at room temperature in which the crystallographic structure is monoclinic, originate from the small size of the Ce^{4+} ion. Two-phase behavior is observed over a large compositional region ($0.1 \leq x \leq 0.167$) at low temperature. The experimental data argue against chemical inhomogeneity or strain arising from grain/domain interaction stresses as explanations for the phase separation. Thus, the extended region of phase coexistence is postulated to originate from the subtle competition among charge, orbital, and spin ordering that may be initiated by A-site cation disorder effect and is then stabilized by an energy barrier between different magnetic ordering that develops in the two phases.

INTRODUCTION

The remarkable transport properties of colossal magnetoresistive (CMR) materials result from strong interactions among charge, orbital, and spin ordering. Thus, detailed knowledge of the structural and magnetic phase diagrams as a function of composition and temperature is fundamental to understanding behavior of these materials. The emerging crystallographic and magnetic phase diagrams show the complex interplay of different ordering phenomena. Examples include the $(Ca_{1-y}^{2+}La_y^{3+})MnO_3$,[1–3] $(Ca_{1-y}^{2+}Bi_y^{3+})MnO_3$,[4] and $(Ca_{1-y}^{2+}Tb_y^{3+})MnO_3$ (Ref. 5) systems. Theoretical work has attempted to explain this complexity in terms of the competition between superexchange and double exchange interactions as well as the effect of the Jahn-Teller distortion rising from the Mn^{3+} e_g electrons.[6,7,8] The ordered states generally found in the $(Ca_{1-y}T_y)MnO_3$ system ($T =$ trivalent ion) are (with increasing y): G- and C-type antiferromagnetic (AFM) structures,[9] the former with a ferromagnetic (FM) component,[1,5,10,11,12] e_g orbital ordering (OO) of the phase associated with the C-type AFM structure,[2,4,13] and charge (CO)- *and* orbital-ordered states when $x \gtrsim 0.2$ mainly attributed to the Wigner-crystal-type ordering.[4,14,15,16] In addition, large areas of phase coexistence are often observed in the previously studied systems. The phase coexistence has been explained to originate from the existence of multiple ground states of comparable energies arising from the subtle competition among the various order-

ing phenomena.[4,5] It has also been proposed that strain fields may stabilize inhomogeneous states.[4,17]

In previous work, $(Ca_{1-x}^{2+}Ce_x^{4+})MnO_3$ was shown to be a two-electron doped CMR system, as followed from the "scaling" of dc magnetic susceptibility with respect to a single-electron doped systems, and from x-ray absorption near-edge spectroscopy data.[18] Single phases were shown to form for $0.0 \leq x \leq 0.175$ by laboratory powder x-ray diffraction. Bulk measurements of the magnetic and transport properties showed rapid changes in the properties with increasing x and the presence of multiple anomalies presumably due to competing AFM, FM, and charge ordering. Apparently, as a result of the high electron doping rate with increasing Ce concentration, the crystallographic and magnetic structures evolve rapidly, leading to a complex structural and magnetic phase diagram. The tentative phase diagram derived in the previous work[18] could not adequately explore this complexity because detailed magnetic structural analysis by neutron diffraction and adequate crystallographic structural data were not available. Therefore, a detailed study of the crystallographic and magnetic phase diagram, by means of neutron and synchrotron x-ray diffraction is needed. Moreover, as has previously been shown for other CMR materials,[19] a knowledge of the evolution of structural characteristics as a function of temperature is essential for understanding the relationship between the structural and electronic properties of these compounds and can provide a guideline for the preparation of new CMR materials with improved properties. A

key objective of the present study was to investigate the role of double charge doping in this class of materials and compare it to the single electron doped systems previously studied, such as $(Ca_{1-y}^{2+}La_y^{3+})MnO_3$ and $(Ca_{1-y}^{2+}Bi_y^{3+})MnO_3$. In the simplest model, one might expect that the $(Ca_{1-x}^{2+}Ce_x^{4+})MnO_3$ phase diagram would simply duplicate the phase diagrams for single-electron doped systems as a function of Mn formal charge state. However, there exist additional factors which may modify the phase diagram. The most evident are the change of average A-cation size affecting the average magnitude of tilting distortion and A-cation size variance, promoting static structural disorder.

We report here the magnetic and crystallographic phase diagram of $(Ca_{1-x}Ce_x)MnO_3$ in the doping range $0 \leq x \leq 0.167$. We show that, to a first approximation, the $(Ca_{1-x}Ce_x)MnO_3$ phase diagram scales to the one-electron doping systems, such that the overall features are very similar as a function of Mn charge state. The specific features that distinguish the studied system from its single-electron counterparts are discussed in detail.

EXPERIMENTAL DETAILS

Powder samples of $Ca_{1-x}Ce_xMnO_3$ ($x=0.025$, 0.05, 0.075, 0.1, 0.125, 0.167) were prepared by a citrate sol-gel method. Stoichiometric amounts of $CaCO_3$ (Aldrich, 99 +%, preheated at 300 °C), $Ce(NO_3)_3$ (0.5 mol/l) and $Mn(NO_3)_2$ (Aldrich, 49.7 wt. % solution in nitric acid) were dissolved in dilute (~ 2 M) nitric acid; then an excess of citric acid and ethylene glycol was added. After all the reactants had dissolved, the solution was heated on a hot plate resulting in the formation of a gel. The gel was slowly heated to 600 °C and left overnight to remove the organic compounds and decompose the nitrates. The resultant powder was pressed into pellets, annealed at 1100 °C for 24 h in air and slowly cooled to room temperature. The samples were shown to be single phase by laboratory powder x-ray diffraction.

Ac susceptibility measurements on ~ 50 mg specimens from all samples were performed with a Quantum Design PPMS 6000 instrument, in the temperature ranges 4–300 K.

Time-of-flight neutron powder diffraction data were collected on the Special Environment Powder Diffractometer (SEPD)[20] at the Intense Pulsed Neutron Source (IPNS) at Argonne National Laboratory. Diffraction data were collected for samples with $x=0.025$, 0.05, 0.1, 0.125, and 0.167 at several temperatures in the range 12–300 K (room temperature). For $x=0.075$, data were collected at several temperatures in the range 4–300 K. Cooling was achieved using a closed-cycle helium DISPLEX refrigerator (brand name of Air Products Systems) to 12 K, and a Leybold refrigerator to 4 K with samples in sealed vanadium cans with helium exchange gas. High-resolution backscattering data ($2\theta = 144.85°$, bank 1), and intermediate-resolution low angle scattering data ($2\theta = 44°$, bank 3), were analyzed using the Rietveld refinement method with the GSAS (EXPGUI) suite.[21,22] 12 K data of the $x=0.125$, and $x=0.167$ compositions were also analyzed using the FULLPROF program.[23]

Form factor coefficients for Mn^{3+} and Mn^{4+} were taken from the International Tables.

High resolution x-ray powder diffraction data were collected on the SUNY X3B1 beamline at the National Synchrotron Light Source, Brookhaven National Laboratory. Data were collected at several temperatures in the range ~ 30–300 K for samples with $x=0.1$, 0.125, and 0.167. Samples were mounted on flat brass sample holders and measured in reflection geometry. Cooling was achieved using a closed-cycle helium DISPLEX refrigerator. The direct synchrotron beam was monochromated by a double Si(111) crystal monochromator at a wavelength of 0.69940(1) Å, as determined from seven well defined reflections of an Al_2O_3 flat plate standard (NIST 1976a). For $x=0.167$, synchrotron x-ray diffraction data taken at 33 K were analyzed using the JANA program.[24]

Small angle neutron scattering (SANS) measurements were performed at the Small Angle Neutron Diffractometer (SAND) at IPNS. This instrument provides data in the Q range from 0.005 to 0.8 $Å^{-1}$ ($Q=4\pi \sin \theta/\lambda$, where 2θ is the scattering angle) in a single measurement by using a 40 $\times 40$ cm^2 position-sensitive ^{3}He gas detector (sample to detector distance $l=2$ m) and neutrons of wavelengths in the range of $\lambda=0.8$ to 14 Å ($\Delta\lambda/\lambda=0.05$ at each λ) by time-of-flight techniques. The powder samples were loaded in Suprasil cells with 1 mm path length and the measurements were performed at different temperatures in the range from 30–300 K. The SANS data are corrected for background scattering for all the samples and are presented on an absolute scale in units cm^{-1} by following the standard procedures at IPNS.[25] In order to extend the data in the low Q region, we measured one powder sample ($x=0.05$) at the USAXS instrument at UNI-CAT beam line at APS and the USANS data at the Perfect Crystal Diffractometer (PCD) at the thermal neutron beam port BT-5 at NIST.

RESULTS AND DISCUSSION

Using the experimental methods described above, a crystallographic and magnetic phase diagram for the $(Ca_{1-x}Ce_x)MnO_3$ system was constructed. The resulting phase diagram is shown in Fig. 1. The following sections of this paper report the details of the data analysis leading to this phase diagram. To aid the reader, we first give a brief overview of the results. In broad terms, the phase diagram can be divided into two regimes. The first regime, for $0 \leq x \leq 0.075$ is characterized by an orthorhombic structure (space-group $Pnma$) at room temperature, and a canted G-type AFM structure at low temperature (magnetic space group $Pn'm'a$). The crystallographic unit cell is $\sqrt{2}a_p \times 2a_p \times \sqrt{2}a_p$, where a_p is the cell parameter of the aristotype perovskite. The second regime, for $0.075 < x \leq 0.167$ is characterized by a monoclinic structure at room temperature ($P2_1/m$; $\sqrt{2}a_p \times 2a_p \times \sqrt{2}a_p$), a C-type AFM structure ($P_{2a}2_1/m$) and, for $0.1 \leq x \leq 0.167$, a CO state of the Wigner-crystal type at low temperatures. In addition, for all $x \geq 0.075$ compositions, phase separated states exist below room temperature, with the phase separation temperature increasing with increasing x. The unit cell of the CO phase follows the general relation ($\sim n \times \sqrt{2}a_p) \times 2a_p \times \sqrt{2}a_p$,
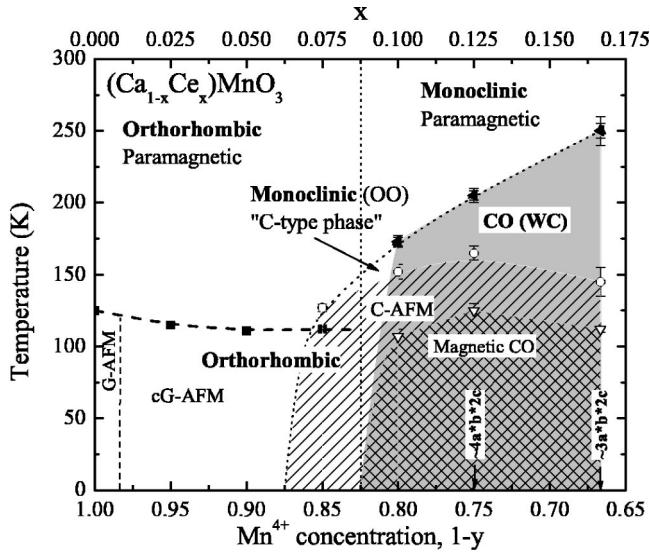
FIG. 1. Crystallographic and magnetic phase diagram for $(Ca_{1-x}Ce_x)MnO_3$ as determined from neutron and x-ray powder diffraction studies. G-AFM, and C-AFM are the G- and C-type antiferromagnetic structures, respectively. cG-AFM, is a canted G-AFM structure. CO is charge-ordered structure. WC is the Wigner-crystal type ordering. OO is orbital-ordering. For the region with $(1-y)<0.85$, overlapping shaded and patterned areas represent coexistence of phases. The area under the thick dashed line $[1 \geqslant (1-y) > 0.825]$ is the area of existence of the G-AFM magnetic structure. The area under the thin dotted line $[0.875 > (1-y) \geqslant 0.66]$ is the area of existence of the C-type monoclinic phase. The diagonal-lines pattern $[0.875 > (1-y) \geqslant 0.66]$ is the area of existence of the C-AFM magnetic structure. The cross-hatched pattern $[0.825 > (1-y) \geqslant 0.66]$ is the area of existence of the magnetic CO structure. The light gray area $[0.825 > (1-y) \geqslant 0.66]$ is the area of existence of the CO phase. Symbols represent transition temperatures measured by methods described in the text. Two specific structures are observed inside the magnetic CO region: magnetic structures with unit cells $\sim 3a*b*2c$ for $x=0.167$ and $\sim 4a*b*2c$ for $x=0.125$. The a, b, and c notations represent the lattice parameters of the original monoclinic unit cell at room temperature.

where $n=(2x)^{-1}$. As an example, for $x=0.167$ (Mn^{3+} content$=\frac{1}{3}$) a CO phase of the Wigner-crystal type exists with $(\sim 3 \times \sqrt{2}a_p) \times 2a_p \times \sqrt{2}a_p$ and a structure similar to that previously observed for $Ca_{2/3}La_{1/3}MnO_3$ (Refs. 14, 15), and $Ca_{2/3}Pr_{1/3}MnO_3$ (Ref. 16). For $x=0.125$ and 0.167 a second magnetic phase, which is associated with the CO phase, is observed below ~ 100 K; it has a $(\sim n \times \sqrt{2}a_p) \times 2a_p \times 2\sqrt{2}a_p$ magnetic unit cell.

In the following text, a detailed presentation of experimental results, their analysis and interpretation from which this phase diagram was created is given. The two-electron doped system discussed here is then compared with one-electron doped systems such as $(Ca,La)MnO_3$, $(Ca,Pr)MnO_3$, and $(Ca,Bi)MnO_3$. Finally, the correlation between magnetic and crystallographic properties is discussed.

Room temperature structures. The room-temperature neutron diffraction spectra of $(Ca_{1-x}Ce_x)MnO_3$ compounds with $0 \leqslant x \leqslant 0.075$ can be fit with an orthorhombic $Pnma$
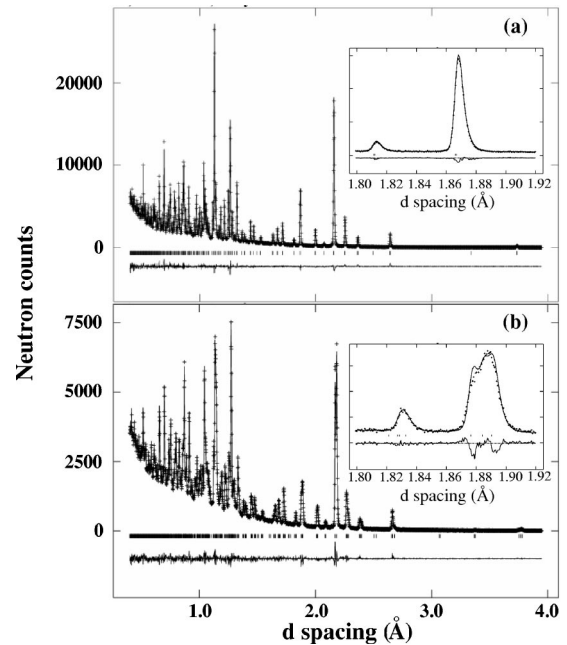

FIG. 2. Time of flight neutron powder-diffraction data ($+$), best-fit Rietveld refinement profiles (solid lines) and their difference (at the bottom) at room temperature for (a) $Ca_{0.975}Ce_{0.025}MnO_3$ ($Pnma$ space-group) and (b) $Ca_{0.833}Ce_{0.167}MnO_3$ ($P2_1/m$). The insets show an example of the peak broadening and splitting upon reduction of symmetry.

structure model with a $\sqrt{2}a_p \times 2a_p \times \sqrt{2}a_p$ unit cell [see Fig. 2(a)]. The room-temperature neutron diffraction spectra of the compounds with $0.1 \leqslant x \leqslant 0.167$ show splitting of reflections in accordance with a monoclinic $P2_1/m$ structure with a similar unit cell [see Fig. 2(b)]. For all samples no deviation from ideal oxygen stoichiometry is found by the refinement of the oxygen atoms occupation factors, using the room-temperature neutron data. Synchrotron x-ray diffraction patterns are consistent with the neutron data. Refinements using the room-temperature synchrotron data allowed a more accurate determination of the Ca/Ce ratio, assuming full site occupancy on the A site, because of the greater scattering contrast between Ca and Ce for x rays than for neutrons. The refinements yielded the nominal Ca/Ce contents within one standard deviation. Refinements of the peak shape parameters yielded nearly instrumental resolution for both neutron and x-ray diffraction patterns, confirming the homogeneity of the samples within the limits of the diffraction method. The cell parameters, atom positions, atomic displacement parameters and reliability factors deduced from the Rietveld refinements using the neutron data are summarized in Table I. Mn-O distances are in agreement with typical values for Mn^{4+}, Mn^{3+}, and O^{2-} assuming a random distribution of Mn^{3+} and Mn^{4+} ions in the B site. Distances are summarized in Tables II and III.

Room-temperature cell parameters of $(Ca_{1-x}Ce_x)MnO_3$ as a function of Mn^{3+} concentration, $y(=2x)$, are shown in Fig. 3(a). A clear change in slope for all three cell parameters is observed upon going from the $0 \leqslant y \leqslant 0.15$ ($0 \leqslant x \leqslant 0.075$) region to the $0.2 \leqslant y \leqslant 0.33$ ($0.1 \leqslant x \leqslant 0.167$) region, in accordance with the transition to monoclinic

TABLE I. Refined structural parameters of $(Ca_{1-x}Ce_x)MnO_3$ at room temperature. Rietveld analyses of neutron diffraction data were done using: For *Pnma* the following atoms positions: $(Ca,Ce)_1$ and O_{11} at $4c(x,1/4,z)$, Mn at $4b(0,0,1/2)$, and O_{21} at $8d(x,y,z)$; For $P2_1/m$ the following atoms positions: $(Ca,Ce)_1$, $(Ca,Ce)_2$, and O_{11} at $2e(x,1/4,z)$, Mn_1 at $2c(0,0,1/2)$, Mn_2 at $2b(1/2,0,0)$, O_{12} at $2e(x,3/4,z)$, and O_{21} and O_{22} at $4f(x,y,z)$. The (Ca,Ce) site is completely disordered. B (U_{ij}) is the isotropic (anisotropic) atomic displacement parameter. B of the two Mn sites in $P2_1/m$ is constrained to the same value. Numbers in parentheses represent standard deviation of the last significant digits. The weighted profile (R_{wp}), and expected (R_{exp}) agreement factors are also given.

X		0.025	0.05	0.075	0.1	0.125	0.167
		Pnma	*Pnma*	*Pnma*	$P2_1/m$	$P2_1/m$	$P2_1/m$
a (Å)		5.2876(1)	5.2981(1)	5.3090(1)	5.3219(1)	5.3351(1)	5.3608(1)
b (Å)		7.4646(1)	7.4759(1)	7.4866(1)	7.4948(1)	7.4989(1)	7.5058(1)
c (Å)		5.2741(1)	5.2823(1)	5.2895(1)	5.2957(1)	5.3016(1)	5.3152(1)
β (°)					90.088(4)	90.120(2)	90.189(2)
V (Å³)		208.17(1)	209.22(1)	210.24(1)	211.23(1)	212.10(1)	213.87(1)
$(Ca,Ce)_1$	x	0.0330(2)	0.0338(2)	0.0344(2)	−0.032(1)	−0.0345(9)	−0.0370(8)
	z	−0.0061(4)	−0.0061(4)	−0.0067(4)	0.007(1)	0.007(1)	0.0069(8)
	B (Å²)	0.63(2)	0.66(2)	0.69(2)	0.8(1)	0.73(9)	0.80(9)
$(Ca,Ce)_2$	x				0.462(1)	0.4615(9)	0.4609(8)
	z				0.494(1)	0.4939(9)	0.4921(9)
	B (Å²)				0.6(1)	0.69(9)	0.67(9)
Mn	B (Å²)	0.22(1)	0.25(2)	0.26(1)	0.24(2)	0.26(2)	0.26(2)
O_{11}	x	0.4897(2)	0.4889(2)	0.4881(2)	0.013(1)	0.0154(8)	0.0157(7)
	z	0.0665(3)	0.0674(4)	0.0684(3)	0.5649(9)	0.5712(8)	0.5743(9)
	U_{11} (Å²)	0.73(5)	0.96(7)	1.02(6)	1.7(3)	1.6(2)	1.7(2)
	U_{22} (Å²)	0.46(5)	0.50(6)	0.50(5)	0.3(3)	0.5(3)	0.6(3)
	U_{33} (Å²)	0.79(6)	0.79(7)	0.81(6)	0.8(2)	0.9(2)	0.8(2)
	U_{13} (Å²)	−0.07(3)	−0.09(4)	−0.07(4)	0.6(2)	0.2(1)	0.0(1)
O_{12}	x				0.487(1)	0.4881(8)	0.4864(7)
	z				0.0737(8)	0.0708(8)	0.0723(7)
	U_{11} (Å²)				0.7(2)	0.8(2)	0.7(2)
	U_{22} (Å²)				0.6(3)	0.5(3)	0.7(3)
	U_{33} (Å²)				0.8(2)	0.7(2)	0.6(2)
	U_{13} (Å²)				0.3(1)	0.1(1)	0.0(1)
O_{21}	x	0.2869(1)	0.2869(2)	0.2874(1)	0.7148(7)	0.7128(5)	0.7105(4)
	y	0.0340(1)	0.0343(2)	0.0349(1)	0.0359(8)	0.0376(6)	0.0359(6)
	z	−0.2875(2)	−0.2877(2)	−0.2879(2)	0.2879(8)	0.2891(6)	0.2902(5)
	U_{11} (Å²)	0.45(2)	0.53(3)	0.61(3)	0.9(2)	1.3(1)	0.5(1)
	U_{22} (Å²)	0.79(3)	0.80(3)	0.85(3)	1.0(3)	1.0(2)	1.1(2)
	U_{33} (Å²)	0.57(2)	0.63(3)	0.65(3)	0.7(2)	0.5(1)	0.8(2)
	U_{12} (Å²)	−0.18(3)	−0.15(3)	−0.16(3)	0.0(2)	0.2(1)	0.4(1)
	U_{13} (Å²)	−0.28(2)	−0.26(3)	−0.28(3)	−0.3(1)	−0.42(8)	−0.44(7)
	U_{23} (Å²)	0.13(3)	0.15(4)	0.16(3)	−0.2(2)	−0.1(1)	0.0(1)
O_{22}	x				0.7898(7)	0.7887(5)	0.7887(5)
	y				0.5352(8)	0.5346(6)	0.5381(6)
	z				0.7887(7)	0.7885(6)	0.7898(5)
	U_{11} (Å²)				0.5(1)	0.20(8)	1.3(1)
	U_{22} (Å²)				0.7(2)	0.8(2)	1.0(2)
	U_{33} (Å²)				0.6(2)	0.9(1)	0.6(1)
	U_{12} (Å²)				−0.2(1)	−0.1(1)	0.3(1)
	U_{13} (Å²)				0.21(8)	0.11(7)	0.11(7)
	U_{23} (Å²)				−0.1(1)	−0.2(1)	−0.4(1)
R_{wp} (%)		4.65	5.45	5.09	4.69	4.07	5.04
R_{exp} (%)		3.03	4.13	3.80	3.65	2.93	3.60

TABLE II. Selected bond lengths (Å) and bond angles (deg.) for Mn octahedra in $Ca_{1-x}Ce_xMnO_3$ ($0 < x \leq 0.075$) at room temperature.

x	0.025	0.05	0.075
$Mn-O_{11}$	1.89956(3)[×2]	1.90348(4)[×2]	1.90732(3)[×2]
$Mn-O_{21}$	1.90290(2)[×2]	1.90622(2)[×2]	1.91173(2)[×2]
	1.90619(2)[×2]	1.91045(2)[×2]	1.91339(2)[×2]
$Mn-O_{11}-Mn$	158.478(1)	158.147(1)	157.807(1)
$Mn-O_{21}-Mn$	157.230(1)	157.101(1)	156.824(1)

symmetry for higher x values. This orthorhombic ($Pnma$) to monoclinic ($P2_1/m$) transition corresponds to a change of the Glazer tilt system from $a^0b^-b^-$ to $a^0b^-c^-$,[26] and apparently originates from the enhanced structural distortion due to the small size of the Ce^{4+} ion, i.e., 1.28 Å in 12 coordinate (1.11 Å in 8 coordinate),[27] in comparison to the size of the Ca^{2+} ion [1.48 Å, 1.26 Å (Ref. 27)]. Consistently, replacing Ca with La^{3+} [1.50 Å, 1.3 Å (Ref. 27)] causes the increase of Mn-O-Mn angles in $(Ca,La)MnO_3$ and the structure approaches cubic symmetry (where the Mn-O-Mn angle is 180°), while replacing Ca with Ce in $(Ca,Ce)MnO_3$ causes the further distortion of the structure (Fig. 3). The reported behavior of the Mn-O-Mn bond angles as a function of y in $(Ca_{1-y}Tb_y)MnO_3$ (Ref. 28), with comparable A cation size (Tb^{3+}: 1.18 Å in 8 coordinate), is very similar to our results [Fig. 3(b)]. However, the room-temperature structure of all studied samples of $(Ca_{1-y}Tb_y)MnO_3$ ($y \leq 0.5$) is reported as orthorhombic with $Pbnm$ space group ($Pnma$ in the standard setting).[28] Moreover, a change of slope in the y dependence of lattice parameters at $y \approx 0.25$ in $(Ca_{1-y}Tb_y)MnO_3$ was observed, especially pronounced for the c lattice parameter.[28] This behavior is similar to our results shown in Fig. 3(b) and suggestive of the orthorhombic to monoclinic reduction in the cell symmetry discussed above for $(Ca_{1-x}Ce_x)MnO_3$, and we believe it to apply for the $(Ca_{1-y}Tb_y)MnO_3$ system as well.

Ac susceptibility. The molar ac susceptibility χ_M as a function of temperature is shown in Fig. 4 for all studied samples. For $0.025 \leq x \leq 0.075$ a Curie-Weiss paramagnetic

TABLE III. Selected bond lengths (Å) and bond angles (deg.) for Mn octahedra in $Ca_{1-x}Ce_xMnO_3$ ($0.1 \leq x \leq 0.167$) at room temperature.

| x	0.1	0.125	0.167
Mn_1-O_{11}	1.90623(3)[×2]	1.91402(3)[×2]	1.91937(3)[×2]
Mn_1-O_{21}	1.90587(6)[×2]	1.91585(4)[×2]	1.92804(4)[×2]
Mn_1-O_{22}	1.91409(6)[×2]	1.91964(4)[×2]	1.93632(4)[×2]
Mn_2-O_{12}	1.91508(3)[×2]	1.91304(3)[×2]	1.91689(3)[×2]
Mn_2-O_{21}	1.92320(6)[×2]	1.92605(4)[×2]	1.92822(4)[×2]
Mn_2-O_{22}	1.92499(6)[×2]	1.92462(4)[×2]	1.93291(4)[×2]
$Mn_1-O_{11}-Mn_1$	158.798(1)	156.738(1)	155.723(1)
$Mn_1-O_{21}-Mn_2$	156.822(1)	155.829(1)	155.484(1)
$Mn_2-O_{12}-Mn_2$	156.134(1)	157.027(1)	156.424(1)
$Mn_1-O_{22}-Mn_2$	156.232(1)	156.631(1)	155.449(1)
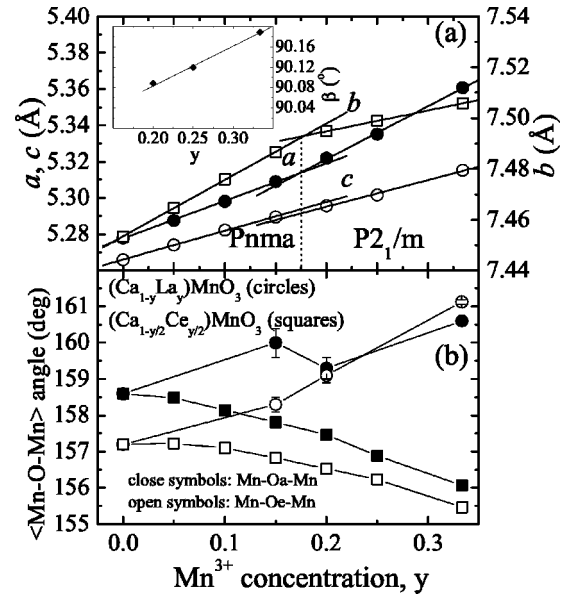
FIG. 3. (a) Cell parameters and (b) average Mn-O-Mn angle at room temperature as a function of Mn^{3+} concentration, $y(=2x)$. Oa and Oe are apical and equatorial oxygen atoms in the Mn-O octahedra, respectively. For $0 \leq y \leq 0.15$ ($0 \leq x \leq 0.075$) Oa and Oe correspond to O_{11} and O_{21}, respectively (Table I). For $0.2 \leq y \leq 0.33$ ($0.1 \leq x \leq 0.167$) Oa corresponds to O_{11} and O_{12}; Oe corresponds to O_{21} and O_{22} (Table I). Data for $(Ca,La)MnO_3$ is taken from Refs. 1 and 14. The inset in (a) shows the variation of the monoclinic angle β with y. Errors are smaller than symbols sizes, unless otherwise shown.

behavior is observed for temperatures above ~ 125 K, while a magnetic transition into an ordered magnetic state occurs at lower temperatures. The sharp rise in the $\chi_M(T)$ curve and drop at slightly lower temperature are suggestive of FM and
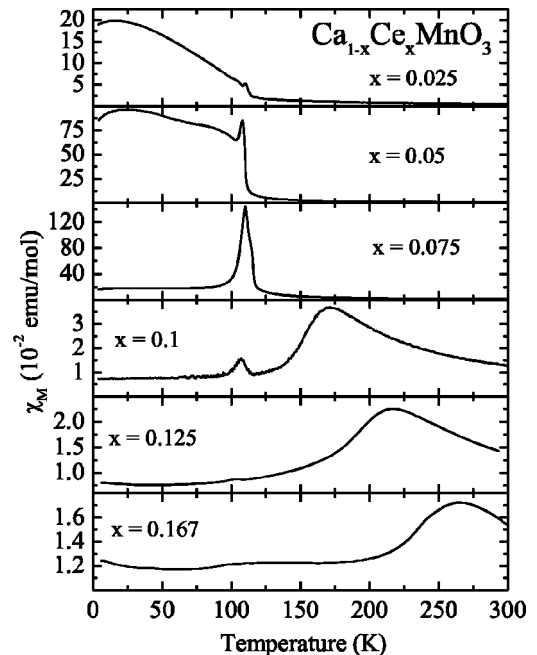

FIG. 4. Molar ac susceptibility as a function of temperature for $(Ca_{1-x}Ce_x)MnO_3$.
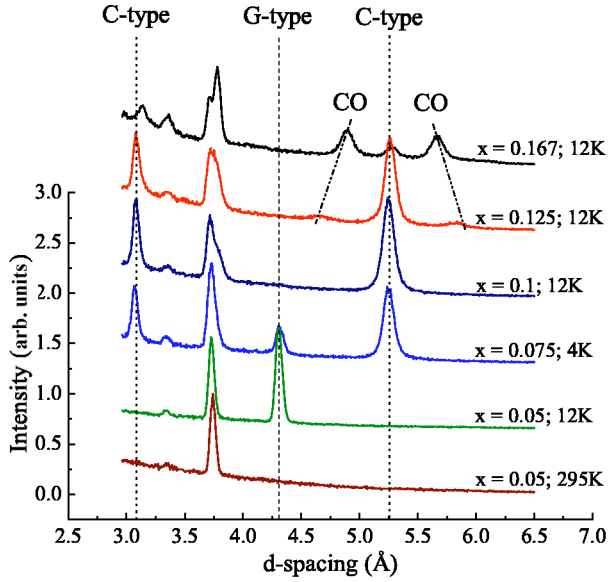
FIG. 5. (Color online). Neutron powder diffraction at 12 K for $0.05 \leq x \leq 0.167$ (at 4 K for $x=0.075$), and at room temperature for $x=0.05$, using data from bank3 ($2\theta \approx 144°$) of the SEPD. CO denotes charge-ordered phase.

AFM transitions, respectively. The neutron diffraction data, discussed in detail below, show that the susceptibility data can be explained in terms of AFM ordering with canting of the moments to produce weak ferromagnetism. For $0.1 \leq x \leq 0.167$ a broad peak is observed in the $\chi_M(T)$ curve at temperatures above 150 K. The peak temperature increases with increasing x (Fig. 4). A small anomaly is also observed at lower temperatures near 120 K (Fig. 4). These results are in a good agreement with the dc magnetization measurements published previously.[18] In that work, the broad peak at temperatures higher than 150 K was shown to correlate with a change of slope in the electrical transport and, therefore, was interpreted as the signature of a CO transition. Additional evidence, showing the correlation of the broad peak in the $\chi_M(T)$ curve with a transition to a CO state as determined by neutron and synchrotron diffraction is given below.

Crystallographic and magnetic properties of $0.025 \leq x \leq 0.075$. Most of the reflections in the 12 K neutron diffraction spectrum of $(Ca_{1-x}Ce_x)MnO_3$ compounds with $x=0.025$ and 0.05 can be fit with an orthorhombic *Pnma* structure model with a $\sqrt{2}a_p \times 2a_p \times \sqrt{2}a_p$ unit cell. Additional reflections observed (see Fig. 5) can be described as a G-type AFM ordering of the Mn sublattice.[9] The magnetic $Pn'm'a$ space-group corresponding to the G-type AFM structure was used to fit the magnetic reflections. In the $Pn'm'a$ magnetic symmetry the G-type AFM structure has Mn magnetic moments aligned along the b axis. In addition, a FM component of the moment, resulting from canting, is possible along the c axis (G_yF_z configuration in Wollan-Koehler[9] notation). Indeed, the refined moment shows a significant FM component along the c axis and the resultant magnetic structure is, therefore, canted G type. This FM contribution is consistent with the sharp rise in χ_M at ~ 115 K observed in the ac magnetic susceptibility for these compounds (Fig. 4). The refined magnetic moments at 12 K for $x=0.025$ and 0.05 are summarized in Table IV.

The canted G_yF_z ($Pn'm'a$) magnetic ordering found here is different from the G_zF_y ($Pn'ma'$) ordering reported for $Ca_{1-x}La_xMnO_3$.[2] The orientation of the magnetic moments with respect to the crystallographic axes is determined by three contributions to the total magnetic anisotropy as described in detail for isostructural (*Pnma*) orthoferrites,[29] namely, magnetodipolar, single ion, and Dzyaloshinskii-Moriya, which are shown to have comparable and often competing contributions to the total anisotropy. All three are shown to be sensitive to the magnitude of structural distortions, and thus it is not surprising that the increased tilt magnitude in $(Ca_{1-x}Ce_x)MnO_3$ as compared to $(Ca_{1-x}La_x)MnO_3$ affects their relative contributions and results in the different observed magnetic structures.

The evolution of lattice parameters and magnetic moments with temperature for the $x=0.05$ sample is depicted in

TABLE IV. Magnetic structures and refined magnetic moments at 12 K, and transition temperatures of $(Ca_{1-x}Ce_x)MnO_3$. MCO is magnetic charge-ordered. T_t^C is the temperature where the C-type phase appears. T_t^{CO} is the temperature where the charge-ordered phase appears. T_N for MCO of $x=0.1$ was determined using the low temperature anomaly in the ac susceptibility measurement.

X		0.025	0.05	0.075	0.1	0.125	0.167
G type	μ_y (μ_B)	2.20(1)	2.21(1)	1.75(4)			
	μ_z (μ_B)	0.47(4)	1.13(2)	1.06(6)			
	T_N (K)	115(2)	111(1)	112(2)			
C type	μ_x (μ_B)			1.65(6)	2.27(5)	2.08(7)	−0.7(1)
	μ_z (μ_B)			−2.34(5)	−2.03(5)	−2.17(7)	1.32(8)
	T_N (K)			127(5)[a]	152(3)	165(5)	145(5)
	T_t^C			127(2)	173(3)	205(5)	250(5)
MCO	μ_{Mn3}					2.0(1)	2.1(1)
	μ_{Mn4}					1.5(1)	1.7(1)
	T_N				107(5)	125(5)	112(2)
	T_t^{CO}				170(5)	205(5)	250(10)

[a]For this compound the C-type magnetic structure appears together with the appearance of the monoclinic C-type crystallographic phase. The estimated C-type magnetic transition from the behavior of the magnetic moment as a function of temperature is 140(5) K.
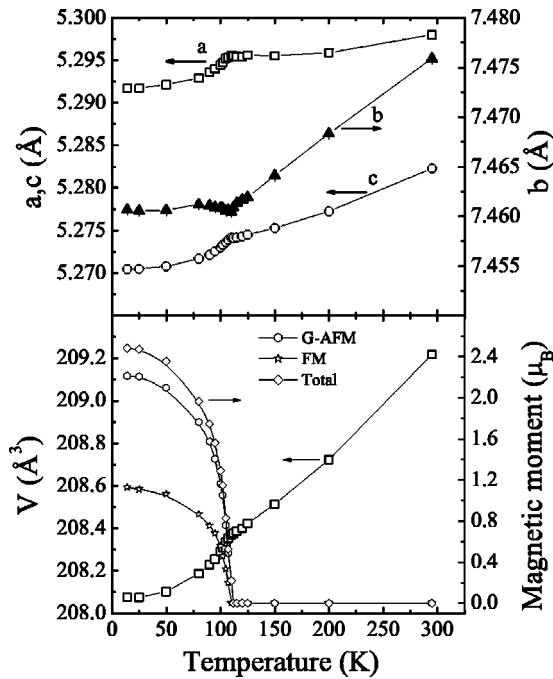
FIG. 6. (top) Cell parameters and (bottom) volume and ordered magnetic moment as a function of temperature for $Ca_{0.95}Ce_{0.05}MnO_3$, determined by Rietveld refinement using neutron diffraction data. Errors are smaller than symbols sizes.

Fig. 6. Similar behavior is observed for the $x = 0.025$ sample (not shown). Lattice parameters values were obtained by Rietveld analysis, using the models described above. In general, all lattice parameters decrease with decreasing temperature. However, a clear anomaly of the lattice parameters is observed in the vicinity of the magnetic transition into the canted G-type AFM structure. The transition temperature as determined by neutron diffraction measurements is 111(1) K (Figs. 1 and 6, Table IV), and is in an excellent agreement with the ac susceptibility measurement (Fig. 4). The behavior of the lattice parameters as a function of temperature (Fig. 6) does not show any evidence of orbital ordering, that typically manifests itself in the expansion of selected lattice parameters when decreasing the temperature due to the cooperative alignment of the e_g orbitals in a selected direction.[4,14]

The 4 K neutron diffraction pattern for $x = 0.075$ shows two coexisting phases (Fig. 5). Reflections can be indexed as coexisting orthorhombic $Pnma$ and monoclinic $P2_1/m$ phases. Two distinct sets of magnetic reflections are also observed (Fig. 5): one corresponds to the canted G-type AFM structure, similar to the one observed for $x = 0.025$ and 0.05, and is indexed using the orthorhombic $Pn'm'a$ magnetic space group (henceforth G-type phase); the other corresponds to the C-type magnetic structure of the Mn sublattice,[9] and is indexed using the monoclinic $P_{2a}2_1/m$ magnetic space group (henceforth C-type phase). The Mn magnetic moments of the C-type phase lie in the ac plane. Their refined values are summarized in Table IV. The refined weight percentage of the monoclinic phase at 4 K is 70%. It is worth noting here that this monoclinic C-type phase is observed in the neutron diffraction data in all studied

samples in the region $0.075 \leqslant x \leqslant 0.167$ (Fig. 5). In addition, the ~ 30 K x-ray synchrotron diffraction data show evidence of this phase for samples in the same composition range.

The evolution of lattice parameters and magnetic moments with temperature for the $x = 0.075$ sample provides additional information about the coexistence of the orthorhombic and monoclinic phases [Fig. 7(a)]. The lattice parameters of the orthorhombic G-type phase show the same temperature dependence as their counterparts in the $x = 0.025$ and 0.05 samples. In contrast to this, the lattice parameters of the monoclinic C-type phase, which appears below 127(2) K, show expansion of the a axis, contraction of the b axis, and contraction followed by expansion of the c axis with decreasing temperature. This behavior is the expected signature[4,5] for orbital ordering of the e_g orbitals within the ac plane. Two distinct magnetic transition temperatures are also observed [Fig. 7(a)]: G-type AFM ordering begins at 112(2) K [Figs. 1 and 7(a), Table IV] while C-type AFM ordering appears at the same temperature where the monoclinic C-type phase appears, i.e., at 127(2) K. The G-type transition temperature as well as the temperature of appearance of the monoclinic C-type phase determined by the neutron diffraction measurements are in excellent agreement with the ac susceptibility results (Fig. 4).

The magnitude of the FM component for the canted G-type AFM structure increases linearly with x (Fig. 8). This results from the increase in the number of FM double exchange interactions of the Mn^{3+}-O-Mn^{4+} type. These double exchange interactions introduce a magnetic frustration to the three-dimensional AFM G-type structure which originates from superexchange AFM Mn^{4+}-O-Mn^{4+} interactions. Eventually, the system tends to stabilize in the C-type AFM structure which is comprised of FM chains. This argument is supported by previously published theoretical work,[7,8] and was previously used to explain the G-type/C-type coexistence in $(Ca_{1-y}Bi_y)MnO_3$ with $y = 0.12$ and 0.15.[4] Other examples of the same coexistence are reported for $Ca_{0.85}Tb_{0.15}MnO_3$,[5] $(Ca_{1-y}La_y)MnO_3$ with $y = 0.1 - 0.16$,[2] and $Ca_{0.9}Pr_{0.1}MnO_3$.[10] The common property of these examples is the Mn^{3+} concentration ($\sim 0.1 - \sim 0.16$).

We mention here that neither of the above discussed phases has 100% abundance at the lowest measured temperature (~ 10 K). In fact, this behavior repeats itself in all studied samples where a phase separation was detected in the $(Ca_{1-x}Ce_x)MnO_3$ system. Moreover, similar phase concentration ratios are found in samples with similar Mn^{3+} concentration, e.g., the C-type:G-type phases ratio for $Ca_{0.85}Bi_{0.15}MnO_3$ at 25 K is $\sim 70\%$:30%,[4] for $Ca_{0.85}Tb_{0.15}MnO_3$ at 16 K it is 79%:21%,[5] for $Ca_{0.84}La_{0.16}MnO_3$ at 20 K it is 81%:19%,[1] and for our $Ca_{0.925}Ce_{0.075}MnO_3$ (0.15 Mn^{3+}) at 12 K it is 69%:31% [Fig. 7(a)]. A possible explanation for the multiple phase state at low temperature in these systems is discussed below after the presentation of results for the rest of the phase diagram. All of the above crystallographic and magnetic findings for $0.025 \leqslant x \leqslant 0.075$ are summarized in the crystallographic and magnetic phase diagram shown in Fig. 1.
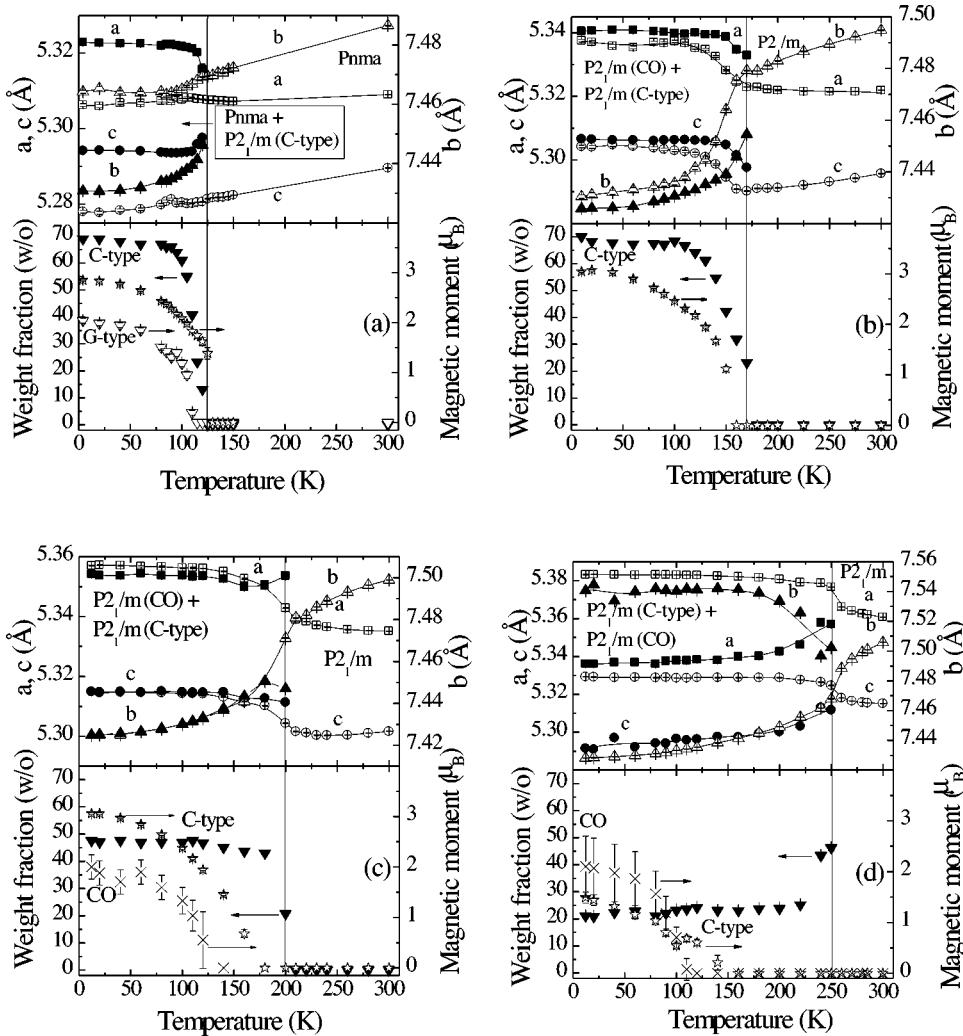
FIG. 7. Cell parameters, *C*-type phase fraction, and ordered magnetic moment as a function of temperature for $(Ca_{1-x}Ce_x)MnO_3$ determined by Rietveld refinement using the neutron diffraction data for (a) $x=0.075$; (b) $x=0.1$; (c) $x=0.125$; (d) $x=0.167$. CO is charge-ordered phase. For cell parameters filled symbols represent *C*-type phase, and open symbols represent (a) *Pnma* phase and (b)–(d) CO $P2_1/m$ phase. The lattice parameters of the CO phase of the $x=0.167$ sample were normalized for comparison with dimensions of the $\sqrt{2}a_p \times 2a_p \times \sqrt{2}a_p$ unit cell. For $x=0.125$ and 0.167, CO magnetic moments as a function of temperature were determined using integrated intensities of magnetic reflections normalized to the value of the Mn^{3+} moment found at 12 K by Rietveld refinement.

Small angle neutron scattering study of x=0.05. In the above analysis and discussion of the magnetic structure of the *G*-type phase, the FM component was modeled using a canted *G*-type AFM structure. However, an important question concerning the FM behavior is whether there is a true

FIG. 8. Ferromagnetic canting angle at 12 K as a function of *x* for the *G*-type antiferromagnetic structure.

canting of the *G*-type AFM structure, as originally proposed by deGennes,[30] or a coexistence of magnetic phase separation to form domains of AFM and FM ordering. Neither experimental nor theoretical work is unanimous on this subject. While the majority of theoretical work supports the phase separated picture for the simple one-e_g orbital model,[6] a recent theoretical work proposes the existence of a stable canted AFM state for small electron doping, when taking into account a twofold degeneracy of the e_g orbitals.[7] Experimentally, while an NMR study of $(Ca_{1-y}Pr_y)MnO_3$ ($y \leq 0.1$),[31] and a SANS study of $(Ca_{0.9}Tb_{0.1})MnO_3$ (Ref. 32) gave evidence of coexistence of FM and AFM clusters, recent neutron scattering work on lightly electron doped $(Ca_{1-y}La_y)MnO_3$ ($0 < y \leq 0.09$) suggested a combined model, which involves a liquid-like distribution of nanometric-size FM clusters (~ 10 Å) embedded in a canted AFM matrix.[1] In addition, in the hole doping regime of $LaMnO_3$, a SANS study revealed the coexistence of ~ 17 Å canted AFM clusters embedded in a matrix of another canted state with different canting degree.[33]

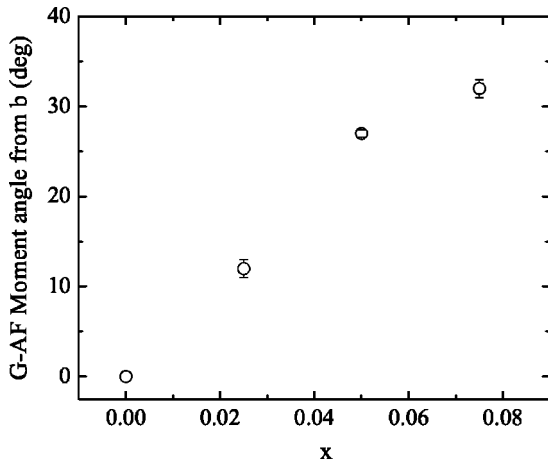In order to resolve this ambiguity in the case of $(Ca_{1-x}Ce_x)MnO_3$ the $x=0.05$ sample was investigated using the SAND instrument at IPNS, ultra-SANS data at the
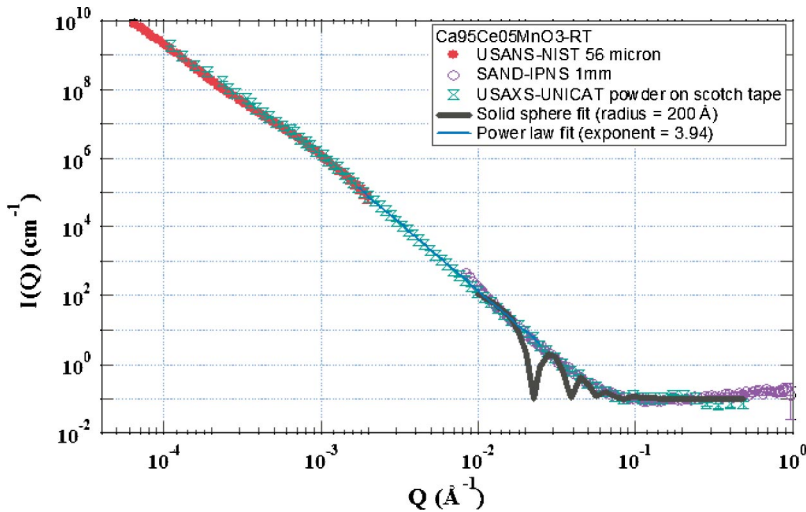
FIG. 9. (Color online). Small angle scattering at RT of the $Ca_{0.95}Ce_{0.05}MnO_3$ sample as seen using neutron scattering on the ultra-SANS at NIST (solid circles), and on SAND at IPNS (empty circles), and x-ray scattering on the ultra-SAXS at APS (up and down triangles). The solid fine line is a fit of the power law model to the data (see text). The thick solid line is a simulation of the scattering expected from solid spheres with the radius of 200 Å (see text).

PCD instrument at NIST, and ultra-SAXS data at UNICAT (33-ID) at the APS at room temperature (Fig. 9). The reason for the use of multiple small angle scattering techniques was twofold: first, to investigate the length scales of all possible inhomogeneities in the system; second, in the case of the x-ray small angle scattering, to compare the neutron results to a nonmagnetic scattering method.

The small angle neutron scattering data at ~ 30 K, measured on SAND at the IPNS, showed no change in comparison to the room temperature measurements shown in Fig. 9, and after normalization, no change between the neutron and x-ray results at room temperature is observed. This result shows that there in no magnetic scattering in the reported Q range. In addition, it is clear from Fig. 9 that large clusters with smooth surfaces or voids with smooth interfaces exist as evidenced by the Q^4 power-law behavior of the scattering over the range $0.001 < Q < 0.01$ (1/Å).[34] The relatively high power estimated in Ref. 1 (~ 5.4) can be understood by the existence of a large multiple scattering in that experiment. Such a multiple scattering occurs when a long wavelength is used to measure the SANS of powder materials. The 12 Å wavelength used in Ref. 1 will promote large multiple scattering. Indeed, in the law Q region in our time-of-flight SANS data (SAND), a $Q^{\sim 6}$ power-law was achieved (not shown), owing to the existence of long wavelengths in that instrument. For data measured using the ultra-SAXS at the APS (~ 1 Å), the PCD at NIST (~ 2.5 Å), and the high Q region measure on SAND (Fig. 9) a Q^4 power-law was achieved.

Based on the presence of a knee in the scattering data at $Q \sim 0.001$ (1/Å) one can estimate[35] the radius of gyration of the clusters to be ~ 2300 Å (Fig. 9)—well within the diffraction limit. The power-law behavior in the low Q region with a slightly smaller exponent may be due to a different type of inhomogeneity in the powders (e.g., particle size). In the high Q region there is no evidence for the presence of clusters with a radius smaller than 200 Å, as is evident from the simulation (solid thick line in Fig. 9), using a spherical particle ("ball") model. Clusters of larger radius (yet still below ~ 1000 Å) would result in a significant broadening of reflections observed by neutron diffraction. No such broadening

was observed for the $x = 0.05$ sample in neither room temperature nor 12 K measurements. Hence, the data reported in this work do not support the presence of FM clusters in an AFM matrix, nor do they support the combined (FM clusters + canted AFM) model suggested previously.[1] In particular, there is no evidence for FM clusters on the scale of ~ 10 Å, as experimentally observed in $(Ca_{1-y}La_y)MnO_3$ with $y = 0.02$ and 0.09.[1] We, thus, interpret our results for the $(Ca_{1-x}Ca_x)MnO_3$ samples with $0 < x \leq 0.075$ solely in terms of a canted AFM model.

Crystallographic and magnetic properties of $0.1 \leq x \leq 0.167$. As was mentioned above, and is summarized in Fig. 1, the entire doping region of $x \geq 0.075$ exhibits phase separation behavior at low temperatures. Additionally, there is an established tendency for the formation of CO states for "commensurate" Mn^{3+}/Mn^{4+} concentration, especially for Mn^{3+} concentrations equal to $\frac{1}{2}$ (Refs. 4, 14–18) and $\frac{1}{3}$ (Refs. 14, 15). Amongst the three studied samples with $x = 0.1$, 0.125, and 0.167, one would expect the 0.167 sample to exhibit the simplest pattern to analyze in the 12 K neutron diffraction data for two reasons: (1) the expected C-type phase concentration is the smallest[4,14] and (2) the unit cell of the CO phase of the $x = 0.167$ sample (Mn^{3+} concentration of $\sim \frac{1}{3}$) is smaller than for $x = 0.1$ (Mn^{3+} concentration of $\sim \frac{1}{5}$) and $x = 0.125$ (Mn^{3+} concentration of $\sim \frac{1}{4}$).[4,14,16] Therefore, we concentrated on understanding the full diffraction pattern of the $x = 0.167$ sample at 12 K, and then used these results to guide analysis of the data for $x = 0.1$ and 0.125.

The 12 K neutron diffraction data for the $x = 0.167$ sample show additional reflections, as well as broadening of selected reflections, in comparison to the room-temperature diffraction data. Following previously published work on samples with an Mn^{3+} concentration of $\sim \frac{1}{3}$ (Refs. 14–16) we were able to index the additional reflections using two magnetic phases: (1) an AFM C-type structure, also observed for $x = 0.075$, and (2) an AFM structure resulting from tripling the a and doubling the c lattice parameters of the original $P2_1/m \sqrt{2}a_p \times 2a_p \times \sqrt{2}a_p$ unit cell (see Fig. 5), and hence presumably originating from the CO phase, which also ex-
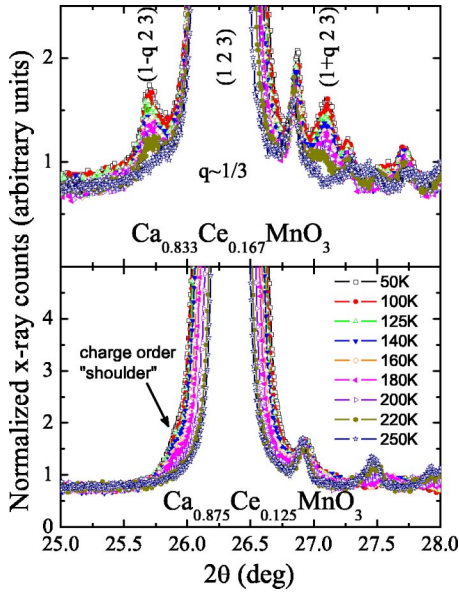
FIG. 10. (Color online) Synchrotron x-ray diffraction data over a selected region as a function of temperature for the $Ca_{0.833}Ce_{0.167}MnO_3$ and $Ca_{0.875}Ce_{0.125}MnO_3$ compounds. The indices of the superlattice reflections of the charge-ordered phase for $Ca_{0.833}Ce_{0.167}MnO_3$ [(2/3 2 3), and (4/3 2 3)] are marked in units of the original unit cell alongside the (123) reflection of the original unit cell. For $Ca_{0.875}Ce_{0.125}MnO_3$ a shoulder reminiscent of charge-ordering superlattice reflection is marked.

hibits tripling of the a lattice parameter (e.g., Refs. 14–16). However, our neutron diffraction data lack the resolution to clearly observe nonmagnetic superlattice reflections from the CO structure.

High resolution synchrotron x-ray diffraction data from the $x=0.167$ sample at ~ 33 K were used to identify the CO superlattice reflections (see Fig. 10). As is clearly observed in Fig. 10, the x-ray diffraction data include additional reflections that can be indexed using a unit cell with dimensions of approximately $\sim 3\sqrt{2}a_p \times 2a_p \times \sqrt{2}a_p$ [$P2_1/m$ space group; propagation vector $(2\pi/a)(\sim\frac{1}{3},0,0)$]. The strongest observed superlattice reflections can be described as first-order satellites of the intense perovskite reflections with nonzero l Miller index [e.g., $(1\pm q\ 2\ 3)$]. Moreover, second-order reflections with Miller indices of $(h\pm 2q,k,l)$ were *not* observed, suggesting that the CO state of the $x=0.167$ sample is of the Wigner-crystal type with transverse modulation, as opposed to a bistripe model, and in agreement with the previously published work on $(Ca_{2/3}La_{1/3})MnO_3$.[14,36] The integrated intensities of the strongest CO superlattice reflections as a function of temperature, obtained from the x-ray diffraction data are depicted in Fig. 11. From this figure the CO transition temperature can be estimated to be $T_{CO}=250(10)$ K. This temperature coincides with the maximum in the $d\chi_M/dT$ derivative of the molar ac susceptibility corresponding to the broad peak observed for $x=0.167$ (Fig. 4).

The superlattice reflections of the CO phase appear to be shifted slightly from the commensurate $3\sqrt{2}a_p \times 2a_p \times \sqrt{2}a_p$ unit cell [see Fig. 12(a)]. Therefore, the peaks were indexed
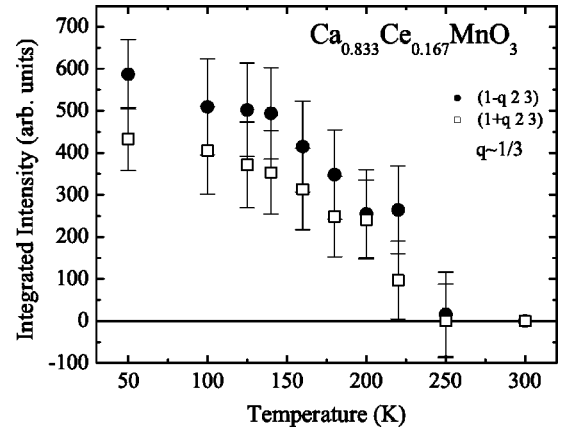

FIG. 11. Integrated intensities of the strongest super-lattice reflections of the charge-ordered phase in $Ca_{0.833}Ce_{0.167}MnO_3$ as a function of temperature.

using the JANA program[24] which is capable of treating incommensurate crystallographic structures. Since the superlattice reflection intensities are less than 1% of the most intense reflections in the pattern, structure refinement was not sensitive to their position, and therefore the Le Bail method was used to fit these reflections. The results are depicted in Figs. 12(a)–12(c). Clearly, the best fit to the data is achieved using modulation along both the a and c directions, giving the propagation vector $\mathbf{k}=[0.315(1),0,0.0269(1)]$. This result is similar to the incommensurate modulation reported for $Ca_{0.67}La_{0.33}MnO_3$ in Ref. 36, where a propagation vector of $\mathbf{k}=(0.284,0,0.01)$ was found by electron diffraction. Incommensurate charge ordering was also found in $Ca_{0.5}La_{0.5}MnO_3$ where an incommensurate-commensurate transition accompanied an AFM-FM one.[37] The difference of the two satellites positions expressed as $\Delta(2\theta)=2\theta_{-\mathbf{k}}-2\theta_{+\mathbf{k}}$, is a measure of the CO propagation vector $\mathbf{k}$. The temperature evolution of $\Delta(2\theta)$ of the CO satellites is shown in Fig. 12(d). Its increase upon cooling is an additional confirmation of the incommensurate nature of the charge-ordering in analogy with the behavior of incommensurate magnetic structures.[38,39]

A Rietveld analysis of the $x=0.167$ neutron diffraction data at 12 K was performed, using the GSAS (EXPGUI) suite.[21,22] The model consisted of two crystallographic phases: (1) a monoclinic $P2_1/m$ phase with a $\sqrt{2}a_p \times 2a_p \times \sqrt{2}a_p$ unit cell, corresponding to the C-type phase similar to that observed for $x=0.075$ and (2) a charge ordered phase. As was mentioned above, neutron diffraction data at 12 K for the $x=0.167$ sample lack the resolution to observe the superlattice reflections of the CO phase. Thus, it is not practical to refine the neutron data using the incommensurate model. Hence, the monoclinic $P2_1/m$ space group with a commensurate $3\sqrt{2}a_p \times 2a_p \times \sqrt{2}a_p$ unit cell is used for the CO phase. Since the crystallographic CO structure is incommensurate, its magnetic structure is incommensurate as well. Therefore, initially, we used in the refinement only the data from the high resolution bank of the SEPD (bank 1; $2\theta\approx 144°$). This approach neglects the small contribution from the magnetic reflections and limits the analysis to the crystallographic
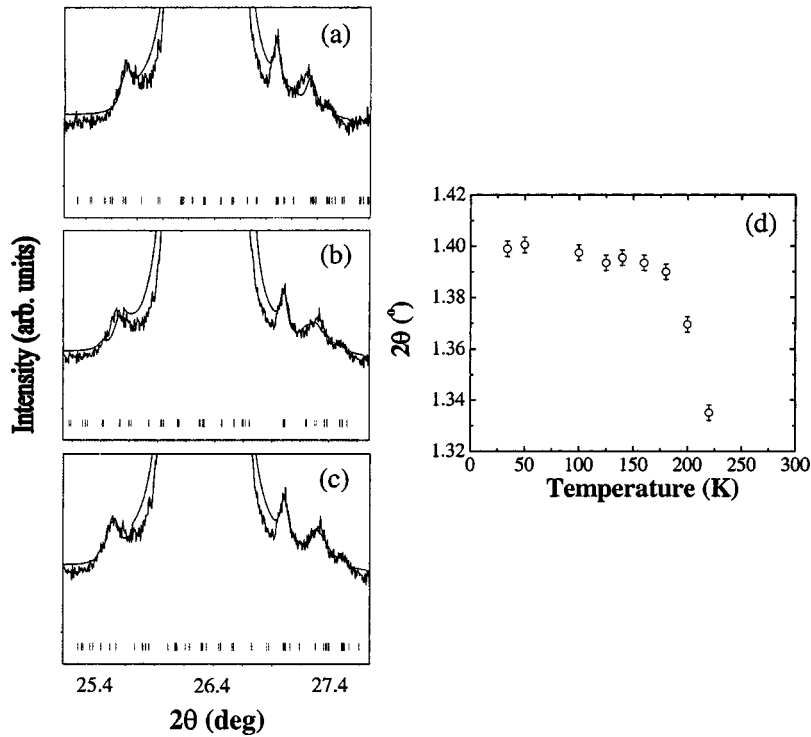
FIG. 12. Observed pattern and Le Bail fit for synchrotron x-ray diffraction of $Ca_{0.833}Ce_{0.167}MnO_3$ with modulation of the monoclinic unit cell $\sqrt{2}a_p \times 2a_p \times \sqrt{2}a_p$ according to the propagation vector: (a) $\mathbf{k}=(1/3,0,0)$, (b) $\mathbf{k}=(0.315,0,0)$, and (c) $\mathbf{k}=(0.315,0,0.0269)$ (see text). (d) Temperature dependence of the scattering angle difference between the CO superlattice satellites corresponding to $\pm\mathbf{k}$.

structure. Then, a detailed treatment of the magnetic reflections was performed as described below. Lattice parameters determined from the synchrotron x-ray diffraction at 33 K and the atom positions previously reported for the $Ca_{0.67}La_{0.33}MnO_3$ sample[14] transformed to the monoclinic $P2_1/m$ structure, were used in the starting model. The decision to use a monoclinic model for the CO phase, rather than the reported orthorhombic model (e.g., Refs. 14, 16) is based on the assumption that this phase originates from the room-temperature phase which already exhibits a monoclinic distortion owing to the small tolerance factor caused by the small ionic size of Ce^{4+}. This assumption is supported by the temperature dependence of the lattice parameters for the $x=0.167$ sample [Fig. 7(d); discussed below]. The refined cell parameters, atom positions, and atomic displacement parameters for the two phases, as well as the reliability factors for the Rietveld refinements are summarized in Table V. The refined phase composition is 80(2)% CO and 20(2)% C type. In comparison, analysis of the 33 K synchrotron x-ray data yields 15(2)% of the monoclinic C-type phase.

Mn-O bond lengths and angles, calculated within the above Wigner-crystal model are summarized in Table VI. All interatomic distances are well within the range for Mn^{3+}-O and Mn^{4+}-O distances in inorganic compounds tabulated in the Inorganic Crystal Structure Database.[40] In particular, bond distances are in good agreement with published distances for $Ca_{0.67}La_{0.33}MnO_3$ which is also charge ordered.[14,15]

Both Mn^{3+}-O octahedra show a classic Jahn-Teller distortion with four short and two long distances. The long bonds are confined to the ac plane, forming an orbital-ordered state, in accord with the observed elongation of both the a and c lattice parameters upon cooling [Fig. 7(d)]. Mn-O-Mn bond angles are significantly smaller than their coun-

terparts in $Ca_{0.67}La_{0.33}MnO_3$,[14] as a result of the large distortion introduced by the small Ce^{4+} ion, and in support of our choice to use a monoclinic system in analyzing the neutron diffraction data for the $x=0.167$ sample.

As was described above, the CO structure of the $x=0.167$ composition is incommensurate. Therefore, the resulting magnetic structure of the CO phase is expected to be incommensurate as well. Indeed the magnetic reflections are shifted from the ideal positions calculated with the commensurate cell. To determine the magnetic structure that best describes the relative intensity ratios of the observed magnetic peaks and estimates the ordered magnetic moments of the Mn^{4+} and Mn^{3+} ions the FULLPROF program[23] was used. The magnetic structure at 12 K for the $x=0.167$ composition can be described as shown in Fig. 13(a) with Mn^{3+} and Mn^{4+} moments of $2.1(1)\mu_B$, and $1.7(1)\mu_B$, respectively (Table IV). It is important to note that due to the large number of nonequivalent Mn positions involved and the incommensuration of the crystal structure we are unable to prove the uniqueness of this structure. However, this magnetic ordering model is consistent with the magnetic structures associated with other previously studied CO phases,[4,14–16] is consistent with our findings for the $x=0.125$ sample, and is in agreement with the orbital ordering in the ac plane. The C-type magnetic structure of the minor phase was also incorporated in the above analysis and the refined moments are summarized in Table IV.

The existence of the CO phase in the $x=0.125$ and 0.1 samples is evidenced by the following observations: (1) the existence of a low temperature "shoulder" on the side of the (123) reflection of the $x=0.125$ synchrotron x-ray diffraction data that can be indexed using a $\sim 4\sqrt{2}a_p \times 2a_p \times \sqrt{2}a_p$ supercell. This "shoulder" disappears above ~ 220 K (Fig. 10).

TABLE V. Refined structural parameters of $(Ca_{0.833}Ce_{0.167})MnO_3$ at 12 K. For *C*-type phase information see Table I. For the charge-ordered (CO) phase Rietveld analyses of neutron diffraction data were done using the monoclinic $P2_1/m$ space group with the following atoms positions: (Ca,Ce), and Oa at $2e(x,\frac{1}{4},z)$, Mn^{4+}, and Op at $4f(x,y,z)$, Mn_{11}^{3+} at $2b(\frac{1}{2},0,0)$, and Mn_{12}^{3+} at $2c(0,0,\frac{1}{2})$. The (Ca,Ce) sites are completely disordered. B (U_{ij}) is the isotropic (anisotropic) atomic displacement parameter. B values of atoms with similar site symmetry are constrained to be the same. Numbers in parentheses represent standard deviation of the last significant digits. The weighted profile (R_{wp}), and expected (R_{exp}) agreement factors are also given.

Phase space-group and name		$P2_1/m$ CO	$P2_1/m$ C
Phase fraction		80(2)%	20(2)%
a (Å)		16.1497(3)	5.336(1)
B (Å)		7.4282(1)	7.541(1)
C (Å)		5.3293(1)	5.2915(9)
β (°)		90.127(3)	91.03(2)
V (Å^3)		639.31(2)	212.88(4)
$(Ca,Ce)_{11}$	x	0.0094(8)	$-0.042(3)$
	z	0.0047(2)	0.025(3)
	B (Å^2)	0.21(3)	0.3(1)
$(Ca,Ce)_{12}$	x	0.5164(8)	0.462(3)
	z	0.511(2)	0.499(3)
	B (Å^2)	0.21(3)	0.3(1)
$(Ca,Ce)_{21}$	x	0.3509(8)	
	z	0.008(2)	
	B (Å^2)	0.21(3)	
$(Ca,Ce)_{22}$	x	0.8447(9)	
	z	0.500(2)	
	B (Å^2)	0.21(3)	
$(Ca,Ce)_{31}$	x	0.6807(9)	
	z	$-0.025(3)$	
	B (Å^2)	0.21(3)	
$(Ca,Ce)_{32}$	x	0.1779(9)	
	z	0.523(2)	
	B (Å^2)	0.21(3)	
Mn_{11}^{4+}	x	0.1697(7)	
	y	$-0.0005(16)$	
	z	0.022(2)	
	B (Å^2)	0.10(3)	
Mn_{12}^{4+}	x	0.6683(8)	
	y	$-0.002(2)$	
	z	0.492(2)	
	B (Å^2)	0.10(3)	
Mn_{11}^{3+}	B (Å^2)	0.10(3)	$-0.06(11)$
Mn_{12}^{3+}	B (Å^2)	0.10(3)	$-0.06(11)$
Oa_{11}	x	0.1645(8)	0.007(3)
	z	0.090(2)	0.576(3)
	B (Å^2)	0.24(3)	0.4(1)
Oa_{12}	x	0.6592(7)	0.481(3)
	z	0.412(2)	0.082(3)
	B (Å^2)	0.24(3)	0.4(1)
Oa_{21}	x	0.4945(7)	
	z	0.094(2)	
	B (Å^2)	0.24(3)	
Oa_{22}	x	$-0.0015(6)$	
	z	0.437(2)	
	B (Å^2)	0.24(3)	
Oa_{31}	x	0.8284(7)	
	z	0.049(2)	
	B (Å^2)	0.24(3)	

TABLE V. (*Continued*).

Phase space-group and name		$P2_1/m$ CO	$P2_1/m$ C
Phase fraction		80(2)%	20(2)%
Oa_{32}	x	0.3232(8)	
	z	0.437(2)	
	B (Å^2)	0.24(3)	
Op_{11}	x	0.0990(6)	0.711(2)
	y	0.035(2)	0.037(2)
	z	0.726(2)	0.300(2)
	B (Å^2)	0.37(2)	0.26(6)
Op_{12}	x	0.5977(5)	0.790(1)
	y	0.036(2)	0.534(1)
	z	0.766(2)	0.799(2)
	B (Å^2)	0.37(2)	0.26(6)
Op_{21}	x	0.0702(5)	
	y	−0.041(2)	
	z	0.215(2)	
	B (Å^2)	0.37(2)	
Op_{22}	x	0.5741(5)	
	y	−0.041(2)	
	z	0.278(1)	
	B (Å^2)	0.37(2)	
Op_{31}	x	0.2348(5)	
	y	−0.038(1)	
	z	0.321(1)	
	B (Å^2)	0.37(2)	
Op_{32}	x	0.7387(5)	
	y	−0.040(2)	
	z	0.193(1)	
	B (Å^2)	0.37(2)	
R_{wp} (%)		4.54	
R_{exp} (%)		2.83	

(2) Broad peaks in the ac susceptibilities for both the x = 0.125 and 0.1 samples with maxima at 218(7) and 170(5), respectively, reminiscent of the same broad peak observed for x=0.167 that was shown to correspond to the CO transition (Fig. 4) (3) The positions of magnetic reflections in the neutron diffraction data at 12 K for the x=0.125 sample which are in agreement with a magnetic $4\sqrt{2}a_p \times 2a_p \times 2\sqrt{2}a_p$ unit cell (Fig. 5). In addition, previously published electronic transport data for x=0.125 and x=0.1 samples were explained in terms of a transition into a charge/orbital ordered state below 225 and 170 K, respectively, in agreement with our findings.

A detailed structural analysis using the synchrotron x-ray and neutron diffraction data including the charge ordering for the x=0.125 and 0.1 samples was not successful due to the reasons stated in the beginning of this section. As an example, attempts to refine a Wigner-crystal model for the x =0.125 sample with a propagation vector of $(2\pi/a)$ $(\sim\frac{1}{4},0,0)$ using the neutron diffraction data failed to converge. An additional complexity in the x=0.125 sample results from the near degeneracy of the (normalized) C type

and the CO phase lattice parameters [Fig. 7(c)], c and b in particular.

The neutron diffraction data for the x=0.125 and 0.1 samples at 12 K were analyzed using a two-phase model which included the C-type phase, as was used for the x =0.167 and 0.075 data, and an average CO phase using the monoclinic $P2_1/m$ space group with a $\sqrt{2}a_p \times 2a_p \times \sqrt{2}a_p$ unit cell. The refined lattice parameters and phase fractions are summarized in Figs. 7(b) and 7(c). The phase ratios of the CO and C-type phases at 12 K are 30(2):70(2)%, and 52(2):48(2)%, for the x=0.1 and 0.125 compositions, respectively. The magnetic ordering at 12 K for the x=0.125 sample can be described by the structure presented in Fig. 13(b) with the Mn^{3+} and Mn^{4+} moments equal to $2.0(1)\mu_B$ and $1.5(1)\mu_B$, respectively (Table IV). However, as for the x=0.167 case described above, it cannot be proven to be unique. The C-type magnetic structure was also incorporated in the above analysis, and the refined moments are summarized in Table IV.

The neutron diffraction data at 12 K for the x=0.1 sample showed no magnetic reflections associated with the CO

TABLE VI. Selected bond lengths (Å) and bond angles (deg.) for Mn octahedra in $Ca_{0.833}Ce_{0.167}MnO_3$ at 12 K, as were calculated using the Wigner-crystal model from Table V.

$Mn_{11}^{4+}-Oa_{11}$	1.90(1)
$Mn_{11}^{4+}-Oa_{31}$	1.89(1)
$Mn_{11}^{4+}-Op_{11}$	1.96(1)
$Mn_{11}^{4+}-Op_{21}$	1.94(1)
$Mn_{11}^{4+}-Op_{31}$	1.93(1)
$Mn_{11}^{4+}-Op_{32}$	1.90(1)
$\langle Mn_{11}^{4+}-O \rangle$	1.92(2)
$Mn_{12}^{4+}-Oa_{12}$	1.92(2)
$Mn_{12}^{4+}-Oa_{32}$	1.89(2)
$Mn_{12}^{4+}-Op_{12}$	1.87(1)
$Mn_{12}^{4+}-Op_{22}$	1.93(2)
$Mn_{12}^{4+}-Op_{31}$	1.87(1)
$Mn_{12}^{4+}-Op_{32}$	1.98(1)
$\langle Mn_{12}^{4+}-O \rangle$	1.91(4)
$Mn_{11}^{3+}-Oa_{21}$	1.926(2)[×2]
$Mn_{11}^{3+}-Op_{12}$	2.031(8)[×2]
$Mn_{11}^{3+}-Op_{22}$	1.925(8)[×2]
$\langle Mn_{11}^{3+}-O \rangle$	1.96(1)
$Mn_{12}^{3+}-Oa_{22}$	1.888(2)[×2]
$Mn_{12}^{3+}-Op_{11}$	2.016(9)[×2]
$Mn_{12}^{3+}-Op_{21}$	1.921(8)[×2]
$\langle Mn_{12}^{3+}-O \rangle$	1.94(1)
$Mn_{11}^{4+}-Oa_{11}-Mn_{11}^{4+}$	157(1)
$Mn_{12}^{4+}-Oa_{12}-Mn_{12}^{4+}$	153(1)
$Mn_{11}^{4+}-Oa_{31}-Mn_{11}^{4+}$	157.1(9)
$Mn_{12}^{4+}-Oa_{32}-Mn_{12}^{4+}$	155(1)
$Mn_{11}^{4+}-Op_{31}-Mn_{12}^{4+}$	150.2(7)
$Mn_{11}^{4+}-Op_{32}-Mn_{12}^{4+}$	155.7(9)
$Mn_{11}^{4+}-Op_{11}-Mn_{12}^{3+}$	157.4(6)
$Mn_{12}^{4+}-Op_{12}-Mn_{11}^{3+}$	158.9(7)
$Mn_{11}^{4+}-Op_{21}-Mn_{12}^{3+}$	152.7(7)
$Mn_{12}^{4+}-Op_{22}-Mn_{11}^{3+}$	157.1(7)
$Mn_{11}^{3+}-Oa_{21}-Mn_{11}^{3+}$	149.3(5)
$Mn_{12}^{3+}-Oa_{22}-Mn_{12}^{3+}$	159.3(6)

FIG. 13. (Color online). Models of Wigner-crystal charge-orbital- and magnetically ordered structures for $(Ca_{1-x}Ce_x)MnO_3$ with $x = 0.167$ (upper) and $x = 0.125$ (lower). Solid, dashed, and waved lines represent ferromagnetic, antiferromagnetic, and frustrated magnetic interactions, respectively.

phase (Fig. 5). Yet, the low temperature anomaly ("small peak") in the ac susceptibility measurement of this sample at ~ 107 K (Fig. 4), suggests the existence of such a magnetic ordering of the CO phase. The magnetic reflections of this phase are expected to be small due to the long periodicity of the magnetic unit cell expected in the $x = 0.1$ cell (unit cell of $\sim 5\sqrt{2}a_p \times 2a_p \times 2\sqrt{2}a_p$). In addition, the CO phase fraction in the $x = 0.1$ sample is 30% at 12 K, resulting in further reduction in the magnetic intensity.

Examination of the proposed magnetic structures for the $x = 0.125$ and 0.167 compositions suggests a possible mechanism for the competition among different electronic ground states in the $0.075 < x \leq 0.167$ composition range of the $(Ca_{1-x}Ce_x)MnO_3$ system. The competition between AFM superexchange and FM double exchange, suggested above for the C-type/G-type competition, can be applied here as well. This competition results in frustration in part of the Mn-O bonds in the CO magnetic structure (Fig. 13). This
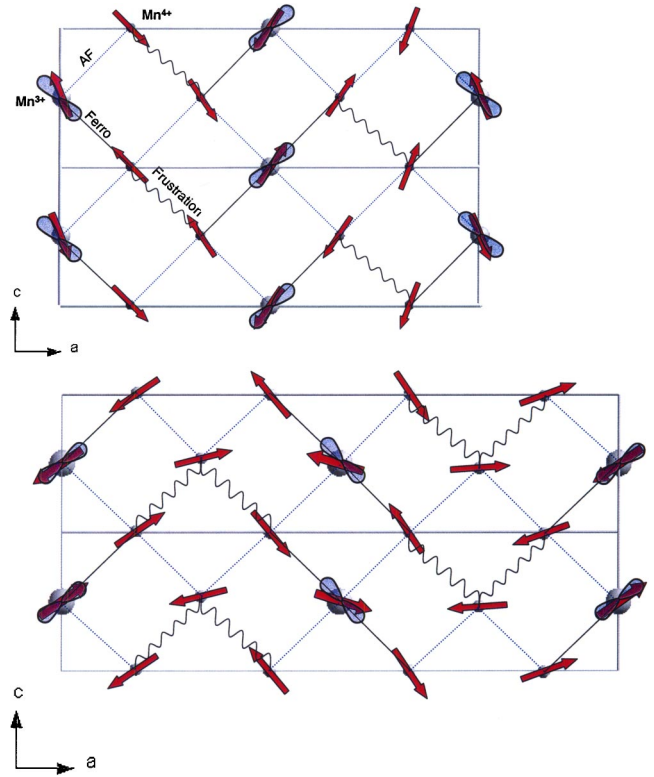
frustration is one of the driving forces for the existence of a multiple ground states resulting in the coexistence of the CO magnetic structure with the C-type one. The concentration of frustrated bonds decreases with increasing Mn^{3+} concentration, tending to stabilize the CO ground state. This hypothesis is in agreement with the monotonic decrease of the C-type phase fraction at 12 K with increasing x in the $0.075 < x \leq 0.167$ region of the $(Ca_{1-x}Ce_x)MnO_3$ system. The same argument was used to explain the behavior of the C-type phase in $(Ca_{1-y}Bi_y)MnO_3$.[4] The multiple ground state caused by the magnetic frustration also explains the relatively low magnetic moments found for the CO magnetic phases (Table IV).

An additional feature that favors magnetic frustration, and therefore the relatively small magnetic moments of the CO phase, is the small value of the Mn-O-Mn bond angles. As is well known, the superexchange interaction weakens as these bond angles vary away from $180°$.[41] This effect was shown previously to cause magnetic frustration in double perovskites.[42] The especially small refined magnetic moment of the C-type phase for $x = 0.167$ [Fig. 7(d), Table IV], where the crystal structure is maximally distorted due to the large amount of the small Ce^{4+} ion, supports this hypothesis.

Evolution of crystallographic and magnetic properties with temperature. Using the models described above, the thermal evolution of the lattice parameters, magnetic moments, and phase ratios of the C-type and CO phases for the

$x = 0.1$, 0.125, and 0.167 samples was determined and is depicted in Figs. 7(b)–7(d) along with results for $x = 0.075$ [Fig. 7(a)]. The lattice parameters of the CO phase of the $x = 0.167$ sample were normalized for comparison with the dimensions of the $\sqrt{2}a_p \times 2a_p \times \sqrt{2}a_p$ unit cell. Clearly, for all three samples ($x = 0.1$, 0.125, and 0.167), the monoclinic phase undergoes a charge- and orbital-ordering transition at lower temperatures as evidenced by the cell expansion upon cooling [Figs. 7(b)–7(d)]. For the $x = 0.1$, 0.125, and 0.167 samples the charge- and orbital-ordering transition temperature is the temperature at which the thermal expansion suddenly changes. This anomaly occurs at the same temperature with the abovementioned broad peaks in the ac susceptibilities (Fig. 4). In addition, a second phase—the C-type phase—appears at the same transition temperature. The evolution of the lattice parameters of the CO phase with temperature implies that the orbital ordering is confined in the ac plane for all three samples, in agreement with the above analysis of the Mn^{3+}-O bond lengths for the $x = 0.167$ CO phase [Figs. 7(b)–7(d), Table V]. The same thermal evolution of lattice parameters has been reported for a variety of CO phases,[4,5,14,15,43] suggesting the same orbital ordering in all studied compounds. The orbital-ordering of the C-type phase is more complex, starting with ordering somewhere within the ac plane for $0.075 \leqslant x \leqslant 0.125$ [Figs. 7(a)–7(c)], and then "switching" to align along the monoclinic b axis [Fig. 7(d)]. At this point we do not have a satisfactory explanation for this effect. However, we note that a similar change in the thermal evolution of the lattice parameters was observed previously in $(Ca_{1-y}La_y)MnO_3$ with $0.1 \leqslant y \leqslant 0.5$,[13] where it was attributed to a switch in orbital-ordering direction with changing y due to fluctuations between the Q_2 and Q_3 modes of the Jahn-Teller distortion.[44]

The C-type phase fraction as a function of temperature is plotted in Figs. 7(b)–7(d). As was the case for the C-type/G-type phases for the $x = 0.075$ sample, neither the CO phase fraction nor the C-type phase fraction reaches 100% at 12 K. In addition, plotting the phase volume of the C-type phase together with the volume of the G-type phase ($x = 0.075$) and the normalized volumes of the CO phases ($0.1 \leqslant x \leqslant 0.167$) at low temperature (Fig. 14) show a linear dependency of the volumes on x and therefore on the Mn^{3+} concentration. But, more importantly, each two phases of the same x value show essentially the same volume, and hence, the *same* charge carrier concentration (Mn^{3+}).

The above experimental findings are in agreement with a theoretical picture in which large clusters of different phases but with the *same* charge concentration coexist at low temperature.[45] A key feature of this model is disorder in the AFM exchange of the t_{2g} electrons and hopping amplitudes of the charge carriers, which is naturally present due to a random distribution of A cations with significant charge and size differences. This type of phase separation is clearly distinct from a more conventional picture of a "droplet" state, with charge carriers being confined within separate domains,[46] and was previously proven to exist in the hole-doped $(La_{1-y}Pr_y)_{0.7}Ca_{0.3}MnO_3$ system in a certain y range by neutron diffraction.[47] The disorder on the A cation site
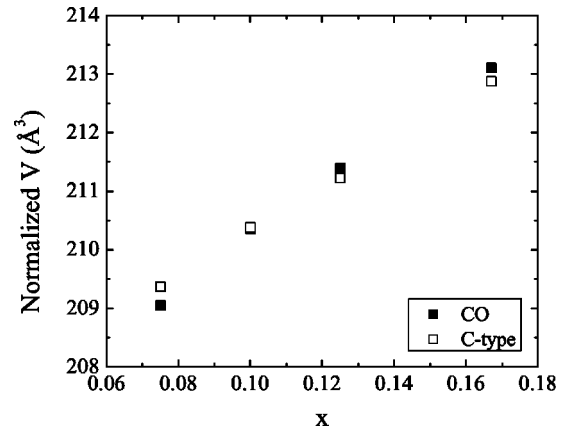

FIG. 14. Unit cell volumes of the charge-ordered (normalized) and C-type phases as a function of x in $(Ca_{1-x}Ce_x)MnO_3$, determined by Rietveld analysis using the neutron diffraction data.

may lead to a distribution of transition temperatures for the crystallites to transform to the C-type phase, since locally the crystal environments are not identical. This creates a "delay" between the initial appearance of the second phase (in our case the C-type phase) and the establishment of its full magnetic ordering, and the establishment (upon further cooling) of the competing state of the original phase, e.g., the G-type magnetic ordering, or the CO magnetic ordering. Once the second magnetic ordering is established, it may create an energy barrier, which prevents the C-type phase from growing further. The end result would be a hindered ability of the system to gain energy by selecting the lowest-energy phase. The system, thus, freezes in its phase separated state. A similar argument was used to explain the multiple phase situation at low temperature in the $(Ca_{1-y}La_y)MnO_3$ system.[2]

Authors in previous work proposed that the inability of the C-type phase to grow to 100% abundance was due to stresses coming from the different thermal expansion of the two phases involved.[17] Such an explanation cannot explain the observations in this work because the observed thermal expansions in the present system would lead to different signs for these stresses at different parts of the compositional phase diagram. As an example, we consider the thermal expansion behavior of the different phases in the $x = 0.075$ and $x = 0.1$ samples [Figs. 7(b) and 7(c)]. For $x = 0.075$, the C-type phase expands in the ac plane upon cooling, and tries to grow into the G-type phase, which contracts in all directions upon cooling. Conversely, for $x = 0.1$, the C-type phase likewise expands in the ac plane upon cooling, but the CO phase in which it nucleates and grows also expands in the ac plane upon cooling. Therefore, the interdomain stresses experienced by the C-type phase are of opposite signs for $x = 0.075$ and $x = 0.1$. However, the observed C-type phase fraction vs temperature is the *same* for these two samples [Figs. 7(b) and 7(c)]. Thus, we conclude that domain interaction stresses arising from the phase transition cannot explain why the transitions result in mixed phases rather than going to completion.

The behavior of magnetic moments as a function of temperature for the C-type and CO AFM structures is also plotted in Figs. 7(b)–7(d). The refined moments and character-
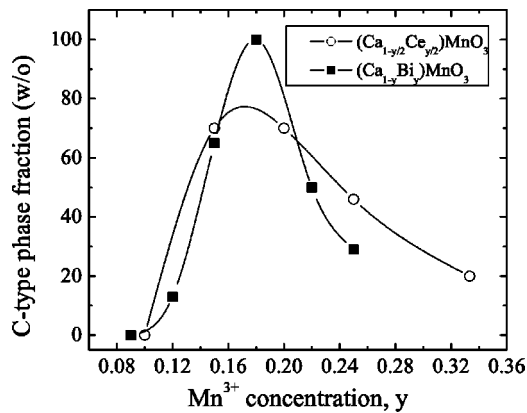
FIG. 15. *C*-type phase weight fraction as a function of Mn^{3+} concentration for the $(Ca_{1-y/2}Ce_{y/2})MnO_3$ and $(Ca_{1-y}Bi_y)MnO_3$ (Ref. 4) systems.

istic temperatures for the entire set of compositions studied are given in Table IV and summarized in the form of the crystallographic and magnetic phase diagram (Fig. 1).

CONCLUSIONS

Neutron and x-ray diffraction data have been used to construct a crystallographic and magnetic phase diagram for the two-electron-doped system $(Ca_{1-x}Ce_x)MnO_3$ (Fig. 1). A comparison of the phase diagram for this two-electron-doped system in the composition range $0 \leq x \leq 0.167$ with phase diagrams for one-electron-doped systems such as $(Ca_{1-y}La_y)MnO_3$,[1,17] $(Ca_{1-y}Bi_y)MnO_3$,[4] and $(Ca_{1-y}Tb_y)MnO_3$,[5] in the corresponding composition range $0 \leq y \leq 0.33$, shows both qualitative (e.g., ordering phenomena) and quantitative (e.g., transition temperatures) similarities. This observation leads to the conclusion, suggested previously,[48] that the crystallographic and magnetic properties of the $CaMnO_3$ based manganites are dominated by the charge state of Mn, rather than by the size of the doping trivalent ion. This similarity even extends to the mixed phase behavior. This conclusion is perhaps best demonstrated by plotting together the *C*-type phase fractions for the $(Ca_{1-x}Ce_x)MnO_3$ and the $(Ca_{1-y}Bi_y)MnO_3$ (Ref. 4) systems vs Mn^{3+} concentration (Fig. 15).

The data presented in this work shed light on the question of whether the large region of phase coexistence observed in so many electron-doped manganite systems is caused by chemical or electronic inhomogeneity. Our diffraction results for single phases at room temperature where all synchrotron x-ray *and* neutron spectra showed no significant peak broadening beyond instrumental resolution argue against chemical inhomogeneity. The remarkably wide region of phase separation is unlikely to be explained by small compositional inhomogeneities not detected by high-resolution diffraction methods at room temperature. As was discussed above, Fig. 14 presents crystallographic evidence of the formation of different phases with the *same* charge carrier (Mn^{3+}) density, again ruling out large chemical inhomogeneity. We therefore attribute the phase separation observed in the $(Ca_{1-x}Ce_x)MnO_3$ phase diagram to an electronic inhomogeneity, driven by the competition between magnetic-charge- and orbital-ordering phenomena.

The low-temperature phase-separated state existing in the studied phase diagram (Fig. 1) in the region $0.075 \leq x \leq 0.167$, can be understood within the framework of the theoretical model presented in Ref. 45, where the *A*-cation disorder was shown to promote the formation of large clusters of different phases with the same charge density. In addition, we show that domain interaction stresses that may originate from the growth of one phase into the other have no significant effect on the properties of the presently studied materials.

*Author to whom correspondence should be addressed. Permanent address: Physics Department, Nuclear Research Center-Negev, P O Box 9001, 84190 Beer-Sheva, Israel.

[1] E. Granado, C. D. Ling, J. J. Neumeier, J. W. Lynn, and D. N. Argyriou, Phys. Rev. B **68**, 134440 (2003).

[2] C. D. Ling, E. Granado, J. J. Neumeier, J. W. Lynn, and D. N. Argyriou, Phys. Rev. B **68**, 134439 (2003).

[3] M. Pissas, G. Kallias, M. Hofmann, and D. M. Többens, Phys. Rev. B **65**, 064413 (2002).

[4] P. N. Santhosh, J. Goldberger, P. M. Woodward, T. Vogt, W. P. Lee, and A. J. Epstein, Phys. Rev. B **62**, 14 928 (2000).

[5] J. Blasco, C. Ritter, J. García, J. M. de Terasa, J. Pérez-Cacho, and M. R. Ibarra, Phys. Rev. B **62**, 5609 (2000).

[6] E. Dagotto, T. Hotta, and A. Moreo, Phys. Rep. **344**, 1 (2001).

[7] I. V. Solovyev and K. Terakura, Phys. Rev. B **63**, 174425 (2001).

[8] S. M. Dunaevsky and V. V. Deriglazov, Phys. Rev. B **67**, 014409 (2003).

[9] E. O. Wollan and W. C. Koehler, Phys. Rev. **100**, 545 (1955).

[10] Z. Jirák, S. Krupička, Z. Šimša, M. Dlouhá, and S. Vratislav, J. Magn. Magn. Mater. **53**, 153 (1985).

[11] K. Hagdorn, D. Hohlwein, J. Ihringer, K. Knorr, W. Prandl, H. Ritter, H. Schmid, and Th. Zeiske, Eur. Phys. J. B **11**, 243 (1999).

[12] H. Fujishiro, M. Ikebe, S. Ohshiden, and K. Noto, J. Phys. Soc.

Jpn. **69**, 1865 (2000).

[13] X. G. Li, R. K. Zheng, G. Li, H. D. Zhou, R. X. Huang, J. Q. Xie, and Z. D. Wang, Europhys. Lett. **60**, 670 (2002).

[14] P. G. Radaelli, D. E. Cox, L. Capogna, S.-W. Cheong, and M. Marezio, Phys. Rev. B **59**, 14 440 (1999).

[15] M. T. Fernández-Díaz, J. L. Martínez, J. M. Alonso, and E. Herrero, Phys. Rev. B **59**, 1277 (1999).

[16] Z. Jirák, C. Martin, M. Hervieu, and J. Hejtmánek, Appl. Phys. A: Mater. Sci. Process. **74**, S1755 (2002).

[17] S.-W. Cheong, P. A. Sharma, N. Hur, Y. Horibe, and C. H. Chen, Physica B **318**, 39 (2002).

[18] Z. Zeng, M. Greenblatt, and M. Croft, Phys. Rev. B **63**, 224410 (2001).

[19] J. F. Mitchell, D. N. Argyriou, and J. D. Jorgensen, in *Colossal Magnetoresistive Oxides*, edited by Y. Tokura (Gordon and Breach Science, Singapore, 2000), pp. 187–236.

[20] J. D. Jorgensen, J. Faber, Jr., J. M. Carpenter, R. K. Crawford, J. R. Haumann, R. L. Hittermann, R. Kleb, G. E. Ostrowski, F. J. Rotella, and T. G. Worlton, J. Appl. Crystallogr. **22**, 321 (1989).

[21] A. C. Larson and R. B. Von Dreele (unpublished).

[22] B. H. Toby, J. Appl. Crystallogr. **34**, 210 (2001).

[23] J. Rodríguez-Carvajal, Physica B **192**, 55 (1993).

[24] V. Petricek and M. Dusek (unpublished).

[25] P. Thiyagarajan, J. E. Epperson, R. K. Crawford, J. M. Carpenter, T. E. Klippert, and D. G. Wozniak, J. Appl. Crystallogr. **30**, 280 (1997).

[26] A. M. Glazer, Acta Crystallogr., Sect. B: Struct. Crystallogr. Cryst. Chem. **28**, 3384 (1972).

[27] R. D. Shannon and C. T. Prewitt, Acta Crystallogr., Sect. B: Struct. Crystallogr. Cryst. Chem. **25**, 925 (1969).

[28] A. Machida, Y. Moritomo, K. Ohoyama, and A. Nakamura, J. Phys. Soc. Jpn. **70**, 3739 (2001).

[29] K. P. Belov, A. M. Kadomtseva, R. Z. Levitin, and A. K. Zvezdin, *Orientational Transitions in Rare Earth Magnets* (Nauka, Moscow, 1979), Chap. 2 (in Russian).

[30] P.-G. de Gennes, Phys. Rev. **118**, 141 (1960).

[31] M. M. Savosta, M. Novák, P. Maryško, Z. Jirák, J. Hejtmánek, J. Englich, J. Kohout, C. Martin, and B. Raveau, Phys. Rev. B **62**, 9532 (2000).

[32] A. Machida, Y. Moritomo, S. Mori, N. Yamamoto, K. Ohoyama, E. Nishibori, M. Takata, M. Sakata, T. Otomo, and A. Nakamura, J. Phys. Soc. Jpn. **71**, 27 (2002).

[33] M. Hennion, F. Moussa, G. Biotteau, J. Rodríguez-Carvajal, L. Pisnard, and A. Revcolevschi, Phys. Rev. Lett. **81**, 1957 (1998).

[34] G. Porod, in *Small-Angle X-ray Scattering*, edited by H. Brumberger (Gordon and Breach, New York, 1967), pp. 1–15.

[35] G. Beaucage, J. Appl. Crystallogr. **28**, 717 (1995).

[36] R. Wang, J. Gui, Y. Zhu, and A. R. Moodenbaugh, Phys. Rev. B **61**, 11 946 (2000).

[37] C. H. Chen and S.-W. Cheong, Phys. Rev. Lett. **76**, 4042 (1996).

[38] M. Kuznietz, P. Burlet, J. Rossat-Mignod, and O. Vogt, J. Magn. Magn. Mater. **69**, 12 (1987).

[39] S. Kawarazaki, M. Sato, and Y. Miyako, J. Magn. Magn. Mater. **153**, 202 (1996).

[40] G. Bergerhoff, R. Hundt, R. Sievers, and I. D. Brown, J. Chem. Inf. Comput. Sci. **23**, 66 (1983).

[41] J. Goodenough, *Magnetism and the Chemical Bond* (Interscience, New York, 1963).

[42] E. N. Caspi, J. D. Jorgensen, M. V. Lobanov, and M. Greenblatt, Phys. Rev. B **67**, 134431 (2003).

[43] A. Llobet, C. Frontera, C. Ritter, M. Respaud, J. M. Broto, M. J. Martínez-Lope, M. A. G. Aranda, and J. L. García-Muñoz, Appl. Phys. A: Mater. Sci. Process. **74**, S1761 (2002).

[44] H. Sawada, Y. Moritkawa, K. Terakura, and N. Hamada, Phys. Rev. B **56**, 12 154 (1997).

[45] A. Moreo, M. Mayr, A. Feiguin, S. Yunoki, and E. Dagotto, Phys. Rev. Lett. **84**, 5568 (2000).

[46] A. Moreo, S. Yunoki, and E. Dagotto, Science **283**, 2034 (1999).

[47] A. M. Balagurov, V. Yu Pomjakushin, D. V. Sheptyakov, V. L. Aksenov, P. Fischer, L. Keller, O. Yu Gorbenko, A. R. Kaul, and N. A. Babushkina, Phys. Rev. B **64**, 024420 (2001).

[48] B. Raveau, A. Maignan, C. Martin, and M. Hervieu, Chem. Mater. **10**, 2641 (1998).